Austenitic parent grain reconstruction in martensitic steel using deep learning

Patxi Fernandez-Zelaia[a,*], Andrés Márquez Rossy[b], Quinn Campbell[a], Andrzej Nycz[a], Christopher Ledford[a], Michael M. Kirka[a]

[a] *Manufacturing Science Division, Oak Ridge National Lab, Oak Ridge, TN, United States*
[b] *Materials Science & Technology Division, Oak Ridge National Laboratory, Oak Ridge, TN, United States*

Abstract

In this work we develop a deep convolutional architecture to estimate the prior austenite structure from observed martensite electron backscatter diffraction micrographs. A novel data augmentation strategy randomizes the global reference coordinate system which makes it possible to train our model from only four micrographs. The model is much faster than algorithmic approaches and generalizes well when applied to micrographs of a different material. Empirical evidence suggests the efficacy of the model depends on the scale of the microstructure and receptive field of the vision model. This work demonstrates that modern computer vision approaches are well suited for capturing complex spatial-orientation patterns present in orientation imaging micrographs.

Keywords:
phase transformations, martensite, steel, machine learning, deep learning

1. Introduction

Allotropic phase transformations occur in many commonly used structural materials. Transformations in steels are perhaps the most studied with many complex microstructures obtainable via different heat treatments and processing routes. In most steels a stable austenite phase forms (γ) from the melt during solidification. Depending on the alloy content and subsequent cooling a

*Corresponding author
Email addresses: fernandezzep@ornl.gov (Patxi Fernandez-Zelaia), marquezae@ornl.gov (Andrés Márquez Rossy), campbellqa@ornl.gov (Quinn Campbell), nycza@ornl.gov (Andrzej Nycz), ledfordcc@ornl.gov (Christopher Ledford), kirkamm@ornl.gov (Michael M. Kirka)

number of different microstructures can be obtained at room temperature. In martensitic steels subject to rapid cooling a transformation takes place from the face centered cubic (FCC) γ to a body centered tetragonal (BCT) martensitic phase α'. In titanium alloys an analogous transformation can take place with $\beta \rightarrow \alpha$. In fields such as welding and additive manufacturing (AM) there is great interest in studying the originally solidified phase structure so as to study the process-structure relations [2, 3, 5, 34]. The difficulty is that the high temperature parent phase must be inferred from the observable child phase. This is typically done by identifying several child-parent crystallographic relationships and then algorithmically reconstructing the unobserved parent phase structure [2, 3, 22].

In the past decade there has been an explosion of research and development in the machine learning (ML) community. This bustling effort has enabled great advances in image processing, natural language processing, data-mining, etc.. Scientists and engineering in other fields have quickly adapted these models for addressing other domain specific challenges. Convolutional neural networks (CNNs) are well suited for analyzing images and so have been repurposed for computer vision (CV) anomaly and defect detection in manufacturing processes such as AM [27, 28, 33, 42–44]. There are a number of works utilizing ML models for segmenting different phases in metallographic images [13, 35]. A few works have even utilized ML for processing the Kikuchi patterns generated in electron backscatter diffraction imaging to aid in the indexing of crystal orientations [15–17]. ML approaches have become ubiquitous in the computation sciences fields for developing computationally efficient surrogate models trained from complex finite element (FE) simulations [20, 38, 39]. Deep learning approaches have been utilized for learning crystal plasticity laws from discrete dislocation simulations [40]. Plasticity models have been effectively trained using purely data-driven procedures which compete reasonably well against traditionally derived plasticity laws [4, 12, 21]. Recent work has even implemented such a model within a user material subroutine in commercial FE software Abaqus [41]. Since gradient information is computed using backpropagation, ML models not only encode the complex physics exhibited by physical simulations but they also capture gradient information about the system. This has enabled a number of researchers to repurpose these networks for solving inverse design or topology optimization problems [7, 9]. This presents an opportunity for massive improvements since ML based topology optimization is not limited by the complexity of the physical simulation. For instance, for density topology optimization the algorithm requires the solid mechanics problem to be limited to the linear elastic regime in order to allow for computation of closed form derivatives of the governing FE equations [30]. In ML there is no such limitation; derivatives are approximated via the architecture and learned model hyperparameters.

There are limited works currently in the literature employing ML approaches towards quantification of spatial orientation data. A number of papers have been published developing CNN models for analyzing Kikuchi patterns but these works focus more on the microscopy aspects of the experiment e.g. indexing the patterns and identifying space groups [15–17]; the joint treatment of spatial-orientation data is not covered. Two-point correlation functions have been established for spatial orientation data on synthetic microstructures [24, 25]. A later work developed an interpretable two-point mean autocorrelation function from experimental EBSD data [11]. A few works have utilized similar

microstructural representations for the development of polycrystalline FE surrogate models [20, 37]. These works are promising as they introduce a novel orientation descriptor that demonstrates remarkable predictive power. The remaining experimental works focus largely on the development of predictive feature descriptors. A magnesium alloy was studied and a decision tree model was built to predict the propensity of grains to nucleate twins during deformation by exploring features distilled from EBSD micrographs such as grain size, neighbor grain characteristics, Schmid factor, kernel average misorientation, etc. [23]. Another work curiously states that use of the Euler angle descriptors, the raw output of EBSD micrographs, is inherently problematic and this seems to be the bottleneck in quantitative analysis of spatial orientation data [19]. These authors also develop a random forest model based on a number of candidate features such as grain shape, misorientation, Schmid factor, Taylor factor, etc.. Very recent work has developed a ML CV model for phase identification from SEM images by using EBSD data as ground truth [29]. However, these authors simply use EBSD to classify phases and the full orientation data is neglected in their analysis.

While there are many works utilizing ML in CV tasks related to other aspects of materials science, to the best of our knowledge no one has addressed the challenge associated with using ML to reconstruct parent grain orientation image maps. That is, given an EBSD image with observable child phase predict the associated unobserved parent phase EBSD image. Furthermore, processing the orientation information present in EBSD image maps is more difficult than gray scale images as the data represents rotational data which must remain physically meaningful and also encode crystal symmetries. In general, works utilizing modern ML CV models to analyze spatial orientation data are sparse and so the topic of study is novel and challenging. In this work we proposed a deep CNN CV model for performing the task of reconstructing prior γ grains from experimental EBSD maps of the α' martensite. We introduce a novel data augmentation strategy which exploits the structure of the orientation data and allows us to train a model from only four micrographs. We find that the model generalizes remarkably well when we test it on large area micrographs from a different alloy produced via a different manufacturing process (AM). Furthermore, it is significantly faster, by orders of magnitude, than the existing algorithmic approaches. However, the efficacy of the model is shown to be sensitive to the ratio of the model's receptive field to the size of α' grains.

2. Methods

The data for training and validation corresponds to martensitic alloy AF9628 [31]. The data is publicly available at `https://petreldata.alcf.anl.gov/` [32]. Four $968.2\mu m \times 424.9\mu m$ EBSD micrographs were utilized for training and one micrograph of the same size for validation. Details on the data augmentation procedure will be described following description of the architecture. Test micrographs were obtained which correspond to wire-arc large area additively manufactured 17-4PH. Samples were metallographically prepared up to a $1\mu m$ diamond suspension finish. Vibratory polishing was performed as a final step using $0.05\mu m$ colloidal silica for $\sim 12\, hrs$. A Zeiss Crossbeam 550 field emission scanning electron microscope with Oxford detectors was used for electron back scatter diffraction (EBSD) imaging.

2.1. Physics based grain reconstruction

Reconstruction of the unobserved parent phase structure is of great importance for studying process-structure relations in processes such as welding and additive manufacturing [2, 3, 5]. For steels there are a number of works in the literature proposing various strategies for inferring parent austenite grains from observed martensitic child structures [2, 22]. The fundamental basis of these approaches is built on the assumption of certain orientation relationships (OR) which describe crystallographic relationships between austenite and martensite. There are several such proposed relationships but the reconstructions used in this work for training our model will focus on a recent work utilizing an iterative method [22]. These author's algorithm is iterative in nature but it most closely follows the Kurdjumov–Sachs (KS) OR. The KS criterion states that $(111)\gamma$ and $(011)\alpha'$ planes and $[\bar{1}01]\gamma$ and $[\bar{1}\bar{1}1]\alpha'$ directions should be parallel.

The algorithm introduced in [22], which is implemented in open source Matlab software *MTEX* [6], instead introduces some flexibility to this criterion. We use the *MTEX* implementation to generate austenite maps which will serve as our ground truth during training. A general description of the procedure will be included here but for a more precise description the reader should refer to the original manuscript. The KS criterion is utilized as an initial guess but these authors develop a more robust model which allows for grain boundary misorientations to deviate slightly from the KS OR. An input image is first processed to identify grain boundaries (given some cut-off misorientation) and the misorientation of each boundary is calculated. These misorientation values are assumed to follow a normally distributed random variable, with the mean corresponding to the KS OR, and thereby this statistical structure allows boundaries to described by a likelihood function. The boundaries are no longer deterministically KS or non-KS, there is a gradation of probability, and this allows for boundaries which are close to the KS OR to be considered in the analysis. All martensitic grains are then utilized to construct a graph; each node represents a grain and adjacent grains are connected with an edge. The edge weight is assigned a value which is related to the likelihood of that particularly boundary being a KS boundary. A Markov clustering algorithm is then used to iteratively manipulate the graph, eliminating weak edges, until the structure becomes stable yielding many clusters. These clusters represent martensitic grains, which share a common parent austenite grain, and from the available information the parent austenite orientation can also be estimated. In the *MTEX* implementation a number of additional steps are also included; filling in of mis-indexed pixels, cleaning of spurious small martensitic grains, cleaning of spurious small austenitic grains, etc.. These steps ensure that no pixels are empty in any of the training, validation, and test images. While this may introduce some error, e.g. pixel orientations which were estimated using information not consistent with the reconstruction algorithm, we found it necessary to include these steps in order to simplify the numerical workflow.

2.2. Rotation representation

In order to build an effective CV model suitable orientation descriptors must first be identified for quantifying the raw data. The standard approach for EBSD data is to specify the local material orientation with Bunge-Euler angles [8]. In this approach each pixel is represented by three angles $\boldsymbol{g} = (\phi_1, \Phi, \phi_2)$

which describe three rotations necessary to map from a global coordinates system to the local crystal coordinate system. Typically the global coordinates system is described by the orientation of the sample inside the microscope (out of plane direction, vertical, and horizontal with respect to the acquired image). While Bunge-Euler angles are intuitively appealing they fail to capture crystal structure symmetries e.g. for cubic materials $(0, 0, 0)$ and $(\pi/2, 0, 0)$ represent identical crystal orientations. This knowledge suggests that perhaps, prior to building and training the CV model, a more appropriate orientation representation is needed. Ideally a mapping (many-to-one) is needed from the Bunge-Euler representation to a representation that does not discriminate between equivalent orientations e.g. $(0, 0, 0)$ and $(\pi/2, 0, 0)$. It is possible that such a mapping could be learned during training but there are a number of approaches in the literature which describe suitable mappings for similar quantification tasks.

For decades basis expansion based approaches have been utilized for describing the crystallographic orientation distribution function (ODF) [8]. Much like how Fourier coefficients can summarize or describe a discrete signal these expansion based methods encode the ODF into a basis weight representation. Since these basis representations are designed for describing crystallographic data they automatically capture crystallographic symmetries. One of these expansions is the generalized spherical harmonics (GSH) representation which has been utilized recently in a number of works for quantifying spatial orientation data. Yabansu et al. [37] utilized GSH in developing a finite element surrogate model for simulating the elastic response of cubic polycrystalline synthetic microstructures. The surrogate consisted of essentially a three-dimensional kernel regression model which behaves like a one layer CNN with no non-linearity. Paulson et al. [24] utilized a GSH representation for developing two-point statistics metrics for digital microstructure representations. In another work Paulson et al. [25] demonstrated that these descriptors can be utilized to correlate structural attributes to the fatigue resistance of different hexagonal closed packed microstructures. In recent work Montes de Oca Zapiain et al. [20] utilized the GSH representation to develop a deep CNN surrogate model for emulating finite element plasticity simulations. An interpretable EBSD-based two-point autocorrelation function was developed by Fernandez-Zelaia and Melkote [11] for experimental work studying the length scale and morphological anisotropy evolution of polycrystalline copper subject to severe plastic deformation. These works demonstrate that the GSH expansion is well suited for quantifying local crystal orientation in spatial data.

The ODF, $f_{\boldsymbol{x}}(\boldsymbol{g})$, can be described for each individual spatial location $\boldsymbol{x}$ as,

$$f_{\boldsymbol{x}}(\boldsymbol{g}) = \sum_{\mu,n,l} F_{l\boldsymbol{x}}^{\mu n} \dot{T}_l^{\mu n}(\boldsymbol{g}), \tag{1}$$

where μ, n, l represent indices for multiple sums, and $F_{l\boldsymbol{x}}^{\mu n}$ is the complex-valued GSH coefficient at $\boldsymbol{x}$. $\dot{T}_l^{\mu n}$ is the corresponding complex valued GSH basis. A detailed description on obtaining these quantities may be found elsewhere [8, 11, 24, 25, 37]. Prior works have shown that for cubic materials 10 terms in the expansion is reasonable [20, 37]. In this work we are not really interested in the ODF rather we simply want to repurpose the basis weights $F_{l\boldsymbol{x}}^{\mu n}$ to represent the local orientation at each pixel. These GSH basis weights can be obtained via a mapping,

$$\boldsymbol{y}_G = s\left(\boldsymbol{g}\right), \tag{2}$$

where the function s takes in the spatial Bunge-Euler data and maps it to the GSH coefficients (hence the subscript G). Note that we omit the indices μ, n, l and simply represent the quantity as a vector. This representation is complex and so for simplicity in implementing the numerical framework we take the 10 complex coefficients and separate them into real and complex parts to yield 20 features. Furthermore, since some of these features are either constant (like the DC offset in a Fourier expansion) or lack a real or an imaginary part we only use the non-trivial features (total of 17).

To demonstrate some of the key points from this section a number of micrographs are shown in Fig. 1. First, an IPF map (out of page direction) is shown for both the observed child martensitic phase and inferred parent austenitic phase. The first Euler angle, ϕ_1, is shown which appears to be noisy and, hence, makes it difficult to visually discern individual grains. However, the two GSH maps clearly highlight all of the grains present in the IPF map. It is reasonable to believe that the unprocessed Euler angles would introduce additional difficulty when training the proposed model architecture.

2.3. Machine learning based grain reconstruction

Since the algorithmic reconstruction of the parent austenite grain is driven by the nature of grain boundaries (KS or near-KS OR) and connecting similarly misoriented features (children of a parent austenite grain) its is plausible to hypothesize that perhaps a convolutional CV model can capture these physical relationships. The architecture should be able to capture features at different scales, for instance different size lathes, while also "connecting" features over long length scales e.g. lathes within one large grain. Hence, we adopt a model based on the U-net architecture which was developed for biomedical image segmentation [26]. The architecture down samples feature maps and then up samples them with some connections allowed between maps of identical sizes. The intuition is that features of different length scales can be learned at different resolutions. Simultaneously the architecture also expands the receptive field of each pixel due to sharing of information between scales. A flowchart of our network is shown in Fig. 2. The input image is convolved four times with 3×3 kernels and 64 filters. Reflective padding is included to maintain identical shapes. Batch normalization follows each convolution operation. Shortcut residual connections are utilized following the first convolution [14]; empirically we observed that this greatly accelerates learning. Following these residual convolution blocks the sample is down sampled using 2×2 MaxPool operations. This is repeated three more times. Then the resulting feature map is up sampled and following each up sampling another residual convolution block of the same structure is applied. This is done until the feature map is $128 \times 128 \times 64$. At each level of up sampling a shortcut residual connection is allowed from the corresponding down sampled feature map. Finally, a fully connected (FC) network with 4 hidden layers maps the depth dimension $64 \rightarrow 256 \rightarrow 128 \rightarrow 64 \rightarrow 17$. A dropout rate of 0.5 was utilized in the FC layers. Layer weights were penalized with penalty coefficient 5×10^{-4}. Leaky ReLu with $\alpha = 0.1$ was used in all activations. The output of the network is the GSH representation of the

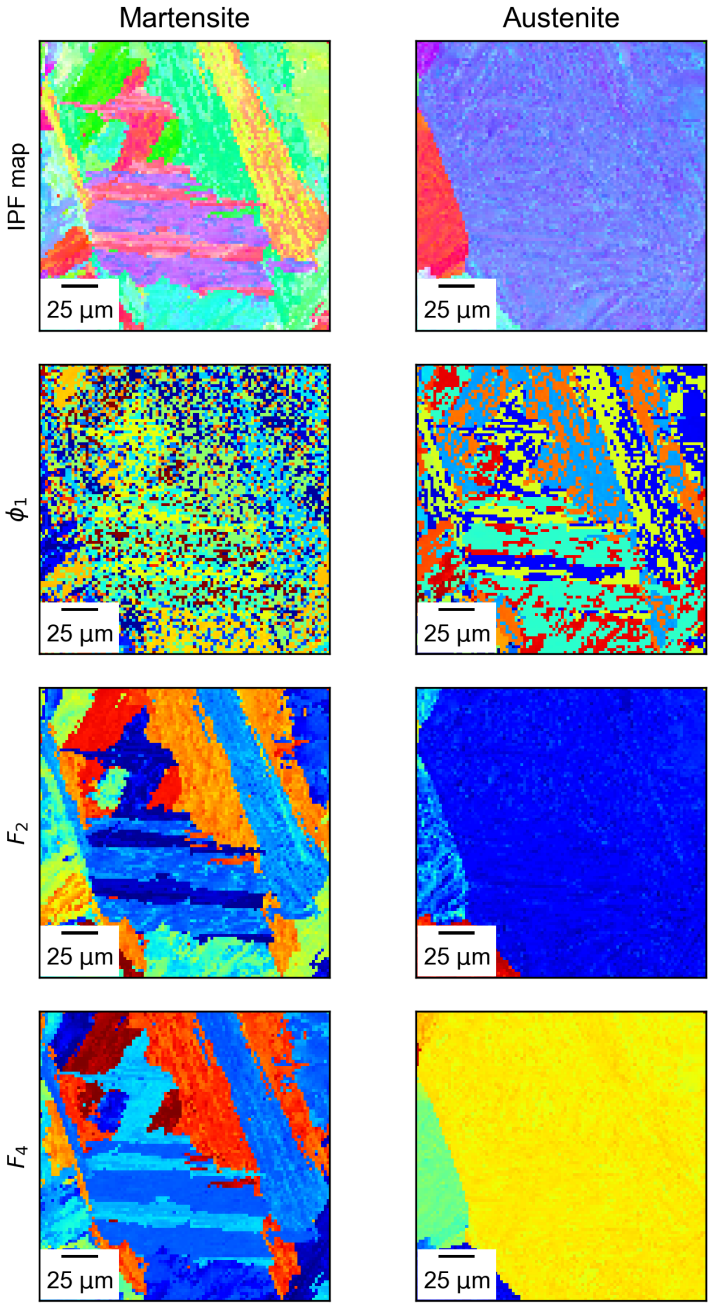

Figure 1: Example micrographs of (left) observed martensitic phase and (right) reconstructed parent austenite phase. IPF map illustrates the out of page orientation. The first Euler angle, ϕ_1, is shown as well as second and fourth GSH coefficient maps for both child and parent phases. GSH many-to-one mapping captures spatial crystal structure more effectively.

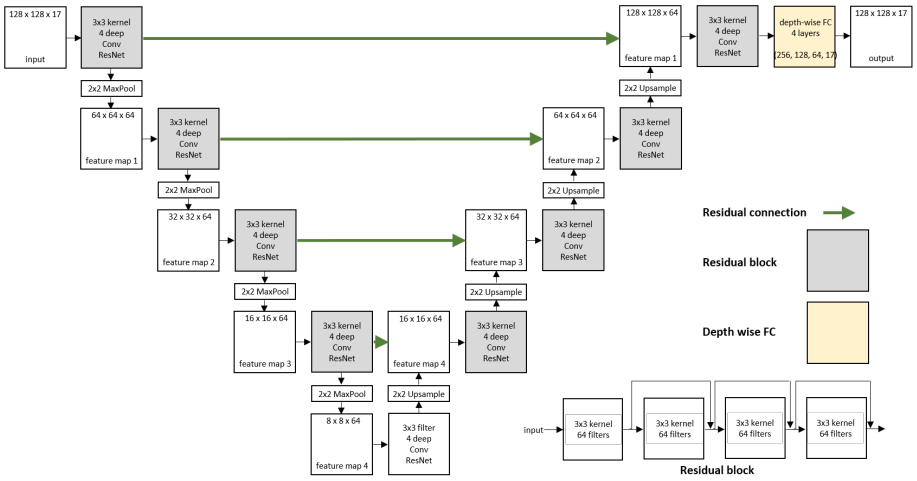

Figure 2: Architecture of the proposed CNN model. The structure generally mimics a UNet architecture but with liberal use of residual connections. Finally, a four layer FC block is utilized in the depth dimension to map each pixel from the latent feature representation to 17 GSH coefficients.

austenite parent grain. A L_2 loss function was utilized to minimize the discrepancy between the ground truth parent austenite GSH representation ($\boldsymbol{y}_G$) and the model's prediction ($\hat{\boldsymbol{y}}_G$).

However, additional effort is needed to produce a model that will yield the desired Bunge-Euler angle outputs $\hat{\boldsymbol{y}}_E$. This representation is needed because it is more amenable for traditional texture analysis (IPF maps, pole figures, etc.). While there is a mapping from the Bugle-Euler angles to the GSH coefficients, to the best of our knowledge the inverse mapping is not as straight forward. Furthermore, the output of the CV model may not even produce physically admissible GSH values, which, despite being "close", would produce nonsensical and complex-valued Bunge-Euler estimates if the inverse transform were available. An analogous operation would be taking the Fast Fourier transform (FFT) of a real signal, then perturbing the coefficients slightly, and inverse transforming back; the reconstructed signal will almost certainly have a significant imaginary component. Hence, another model needs to be learned which maps from the estimated GSH representation to realistic Bunge-Euler angles. This mapping can be described by,

$$\hat{\boldsymbol{y}}_E = h\left(\boldsymbol{y}_G\right), \tag{3}$$

where h is a learnable function (a neural network). We use a FC model with 6 hidden layers each with 128 units except the last which has three units (for the Bunge-Euler angles). Training can be performed by minimizing the following loss function,

$$loss = \sum_i \exp\left(-\left\|\boldsymbol{y}_{G,i} - \hat{\boldsymbol{y}}_{G,i}\right\|^2\right)\left[s\left(h\left(\hat{\boldsymbol{y}}_{G,i}\right)\right) - \hat{\boldsymbol{y}}_{G,i}\right]^2, \tag{4}$$

where s is the function that transforms Bunge-Euler angles into the GSH coefficients. The $\exp\left(\ldots\right)$ is a weighting function which penalizes pixels which are

poorly predicted by the CV model. This was found to be helpful in training h since otherwise the model will be biased by data in regions where poor GSH values are predicted. The nested structure forces the network to learn a mapping h which generates Bunge-Euler angles which in turn produce reasonable GSH coefficients. This may seem confusing but it is necessary; s is a many-to-one mapping so the inverse is not truly a function. However, keep in mind that there is non-uniqueness associated with the Bunge-Euler representation and so this apparent problem really doesn't matter; in this case there is no "right" answer. There are several Bunge-Euler representations which can be "picked" for a given GSH feature vector and they all represent the same crystal orientation. Under this interpretation h is really more of a sampler and this procedure simply ensures that h picks one of the many suitable Bunge-Euler angles. This model was trained separately from the CV model using the Adam optimizer and a learning rate of 10^{-3}.

There is one final complication that must be resolved prior to moving forward. The function s must be differentiable in order to learn the hyperparameters associated with h using gradient based methods. Unfortunately, while that function has real inputs (Bunge-Euler angles) and considered to also have real outputs (10 GSH complex coefficients converted to 17 real values), the computations involve complex numbers. This complicates the theory somewhat but significantly affects numerical implementation. Out of curiosity we simply tried to emulate this function with yet another FC network and it worked reasonably well. In this case the FC network consists of 7 layers each with 128 units except the final layer which has 17 units (for 17 GSH coefficient features). Training was performed separately using the Adam optimizer and a learning rate of 10^{-3}. The training procedure involved randomly generating one million Bunge-Euler angles, computing the GSH representations, and then reducing the corresponding L_2 loss.

In summary three models are introduced and described in this section,

1. A convolutional deep neural network with a U-net structure which makes liberal use of residual connections. The input into this model are child phase martensite micrographs ($128 \times 128 \times 17$) represented using GSH expansion basis weights. The output is a micrograph of identical shape which estimates the GSH representation micrograph of the parent austenite phase.
2. A fully connected neural network which maps each pixel in the estimated parent austenite GSH micrograph to Bunge-Euler angles.
3. A fully connected neural network that emulates the Bunge-Euler to GSH mapping. This function is somewhat a of a nuisance since it is really only needed during training of the prior network. It is necessary since it is difficult for gradients to flow through the true function which maps Bunge-Euler angles to GSH coefficients.

An illustration of these three models is shown in Fig. 3.

2.4. Data augmentation & training

Training was performed using four publicly available $968.2\mu m \times 424.9\mu m$ EBSD micrographs with a native resolution of $0.5\,\mu m$ [31, 32]. Through experimentation we found that a 128×128 sample at $2\,\mu m$ resolution was suitable

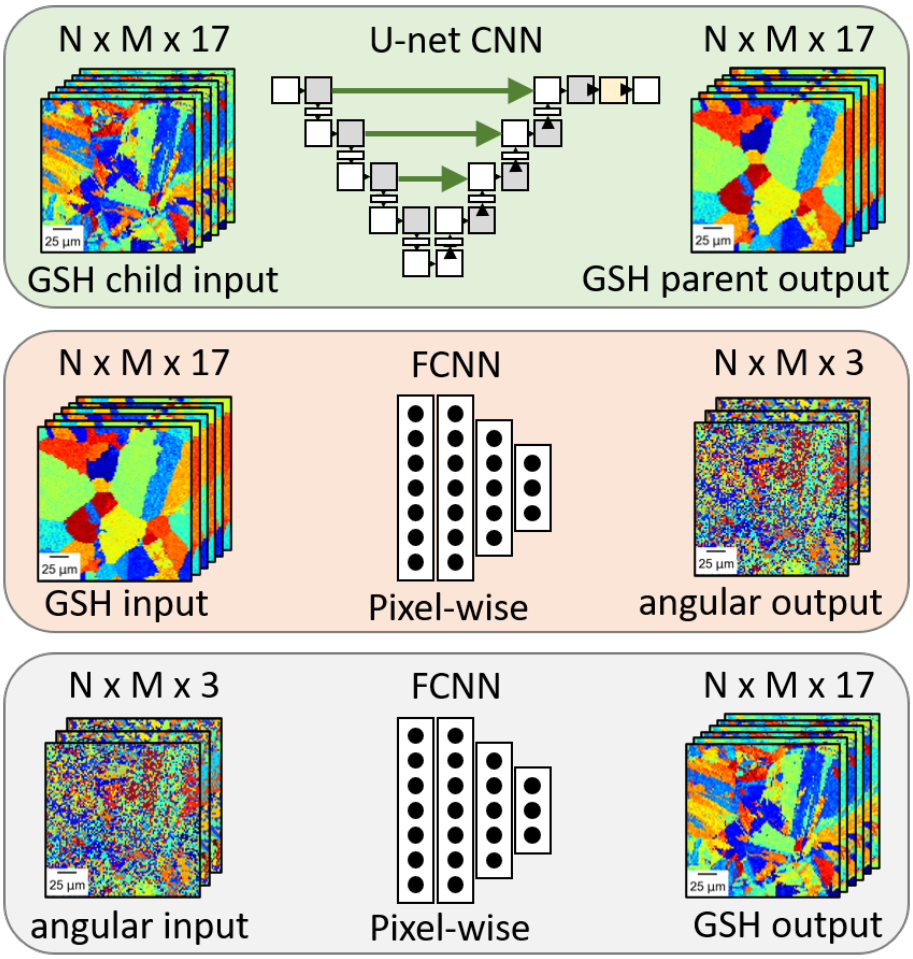

Figure 3: Schematic illustration of the three models proposed in this work. The final model is purely needed for convenience during training of the second model. The FC models operate on image in a pixel-wise fashion.

for training. The data set was augmented by sub-sampling images subject to random spatial rotations. Note that in natural images interpolation is trivial since colors are indeed physically continuous. However, this is not true of the GSH representation; averaging two GSH basis weights may yield a weight which is physically inadmissible. Furthermore, interpolation may be dangerous when considering EBSD micrographs since grain boundaries are sharp; we found that naive interpolation introduces artificial smoothing on grain boundaries. Therefore, we utilized a nearest neighbors interpolation approach for random spatial rotation of the GSH feature maps. More simple augmentation operations were done on the fly during training. This includes flipping of the image (up/down, left/right) and injection of a small amount of noise $\mathcal{N}(0, 0.1)$. Note the injection of noise does also produce some non-physical values but we found that this effect not to be deleterious and, more importantly, it does not bias grain boundary pixels like continuous interpolation.

In addition to the above augmentation strategies we also utilized a novel operation specific for this niche application; random *orientation* rotations. Recall that each pixel represents a rotation that maps the local crystal coordinate system to a reference global coordinate system. Hence, a random orientation rotation can be applied over the entire image (pixel by pixel) to yield a "new" micrograph. This micrograph represents the orientation data relative to a *random reference coordinate system*. Since the choice of global coordinate system is arbitrary this is a reasonable operation. Furthermore, since the orientation of each pixel is rotated identically, the relative misorientation across grain boundaries is preserved. Since the parent phase is inferred via analysis of the grain boundary misorientations, which are unaffected by the absolute orientations of grains, then this operation should be effective at augmenting the data set and will enable learning of a more robust CV model. This random rotation is implemented by first sampling three random angles,

$$\phi_1', \Phi', \phi_2' \sim unif\,(0, 2\pi) \tag{5}$$

which represent the random transformation in Bunge-Euler angles. Next, consider that at each pixel the Bunge-Euler angles represent the rotation necessary to map from the global to the crystal coordinate system. Hence, the procedure will be to (1) map from the crystal coordinates back to the global coordinate, and then (2) randomly rotate the global coordinate with $(\phi_1', \Phi', \phi_2')$. Using z-x-z (ϕ_1, Φ, ϕ_2) ordering the rotation matrix describing this operations is

$$\boldsymbol{R}_{\boldsymbol{x}} = \boldsymbol{R}^T_{\phi_2,\boldsymbol{x}} \boldsymbol{R}^T_{\Phi,\boldsymbol{x}} \boldsymbol{R}^T_{\phi_1,\boldsymbol{x}} \boldsymbol{R}_{\phi_1'} \boldsymbol{R}_{\Phi'} \boldsymbol{R}_{\phi_2'} \tag{6}$$

where $\boldsymbol{x}$ in the subscript indicates that the quantity is spatially dependent e.g. at each pixel. $\phi_{1,\boldsymbol{x}}$ indicates the first Bunge-Euler angle at spatial location $\boldsymbol{x}$. Rotation matrices are about either x or z coordinate axis indicated by the Bunge-Euler angle subscript. The randomly drawn angles are not spatially dependent because the entire micrograph, both child and parent images, must share the same reference coordinate system. The resulting rotation matrix represents the orientation of each pixel relative to a random reference coordinate system. Bunge-Euler angles corresponding to this rotation matrix can easily be extracted. We used the implementation provided by *Python* scientific computing library *SciPy* (scipy.spatial.transform.Rotation) [36].

In Fig. 4 we show one of the training micrographs and three random rotations of a selected 128×128 patch. Both the child martensite and parent austenite samples are shown. The spatial structure is identical in these three examples but clearly the absolute orientation is perturbed in each micrograph.

A total of 7,000 $128 \times 128 \times 17$ micrographs were generated for training using the above procedures. The architecture was implemented in *Python 3.7* using *Tensorflow 2.0* [1]. Training of the CV model was performed using the *Adam* optimizer with default parameters and a learning rate of 5×10^{-4} [18]. A relatively small batch size of 16 was utilized. All training was performed on a single Nvidia Quadro RTX 5000 with 16GB of RAM.

3. Results

In Figs. 5 & 6 two samples from the validation data set are shown. In the first row are micrographs corresponding to three GSH feature maps. The middle row is an IPF map (out of plane direction) corresponding to the ground truth *MTEX* physics reconstruction. The bottom row is an IPF map of the reconstruction using our ML CV model. Overall the CV model reconstructions are fairly good. With a few exceptions the general parent austenite grain shape is recovered, although, on occasion, there is a fictitious grain boundary or slightly misplaced boundary. Most notably the CV reconstruction appears to have a significant amount of within-grain internal misorientations. This is perhaps most clear in Fig. 6 which contains a few large grains. The internal misorientations, while visually unappealing, appear to match the variation from noise present within grains in the physics reconstruction. It is as if the CV model realizes that there will be variability in the reconstructed grain but erroneously "spreads" the variation over large length scales. In the physics reconstructed grains the noise is pixel-to-pixel whereas variation in the CV reconstruction gyrates over many pixels.

In order to test the model's ability to generalize the learned crystallographic spatial patterns we utilized it to reconstruct a completely different martensitic system produced via a different process. Shown in Fig. 7 are micrographs from 17-4PH fabricated via large area wire-arc AM. IPF maps in x,y, and z directions are shown for the observed martensite, physics reconstruction, and ML reconstruction. The input image was $1\mu m$ resolution and 800×800 pixels. The reconstructions in this case are remarkably good. There are a few misplaced grains but in general both the morphology and crystallographic texture of the ML reconstruction are accurate.

The 17-4PH micrographs are again shown in Fig. 8 but this time a $256\mu m \times 256\mu m$ region is magnified to highlight smaller scale features. Furthermore, the resolution of the input image is decreased by a factor of 4 and 8 to empirically evaluate the efficacy of the model to generalize to coarser images. Again, the model performs remarkably well at making predictions on coarser images. This, however, is not particularly surprising. Firstly, the model does not know about physical scale it simply operates on pixels. What is important is the model's *receptive field*, that is, how much of the surrounding area the model can "see" when making a prediction at a individual pixel. Assume that the receptive field of the model is constant e.g. perhaps 100×100 pixels. When the resolution is decreased then more and more microstructural features will fit within the receptive field ($\sim 100 \times 100$) and so there is more context available for predicting

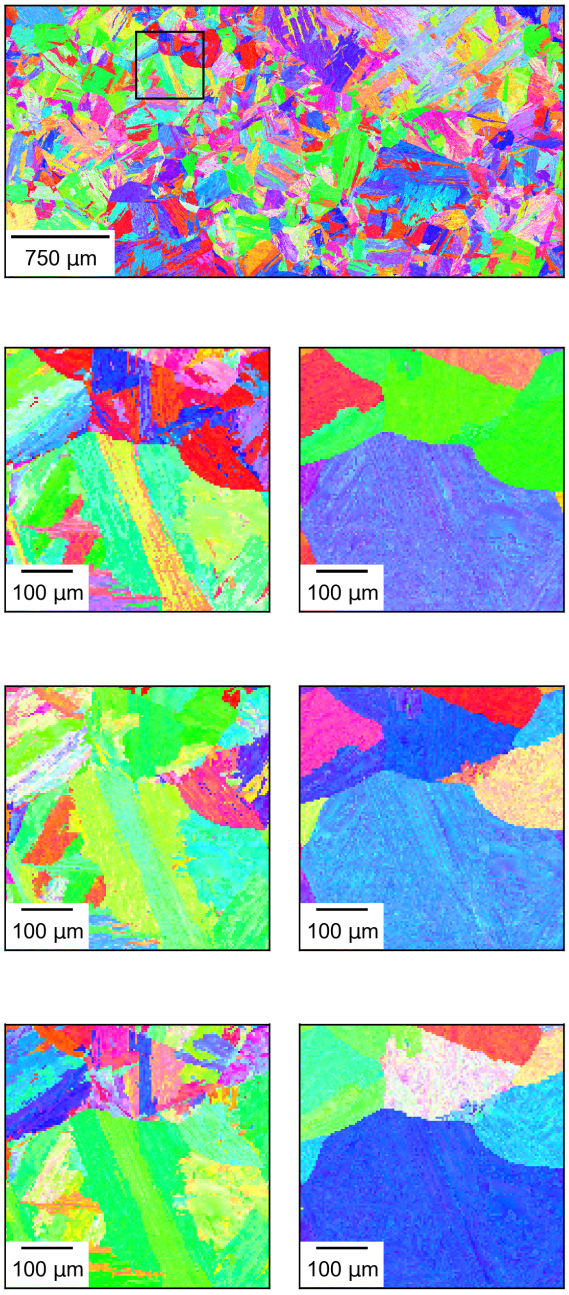

Figure 4: All IPF maps shown out of page orientation. (top) One of four training micrographs. Highlighted is a 128 × 128 window corresponding to micrographs below. Below are three realizations of (left) the martensitic child phase and (right) the austenitic parent phase. For each pair of (child,parent) micrographs each pixel's rotational representation is randomly rotated to generate additional synthetic data. Boundary misorientations are preserved through this transformation while absolute orientation is changed. This emulates the randomization of the global reference frame.

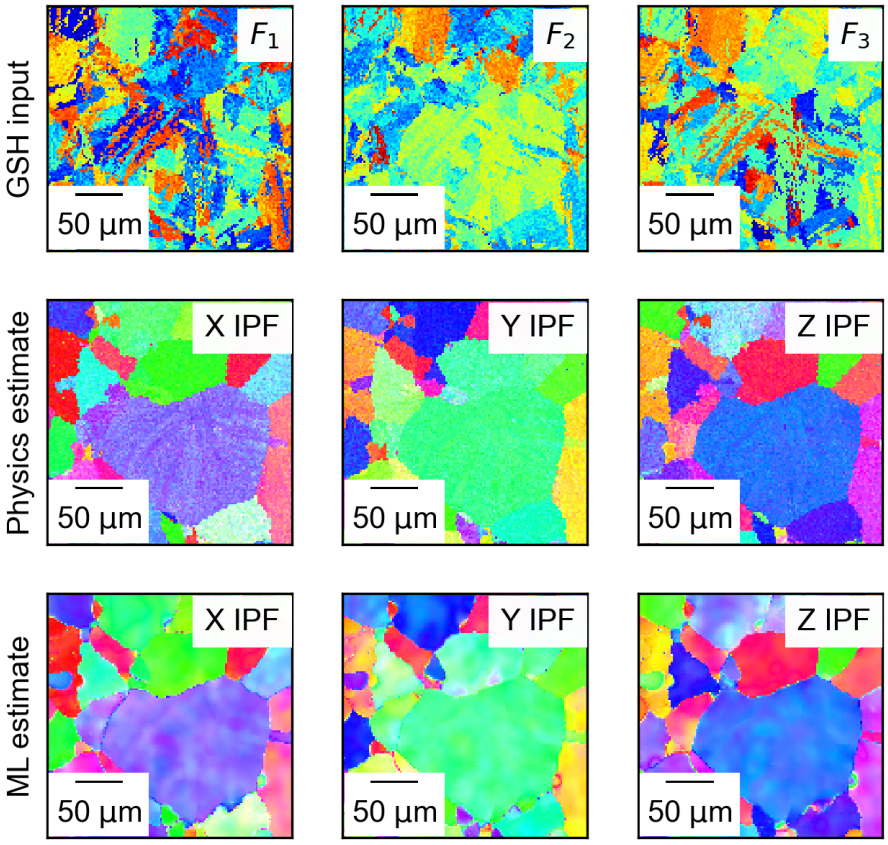

Figure 5: Validation data set example including mostly small scale grains.

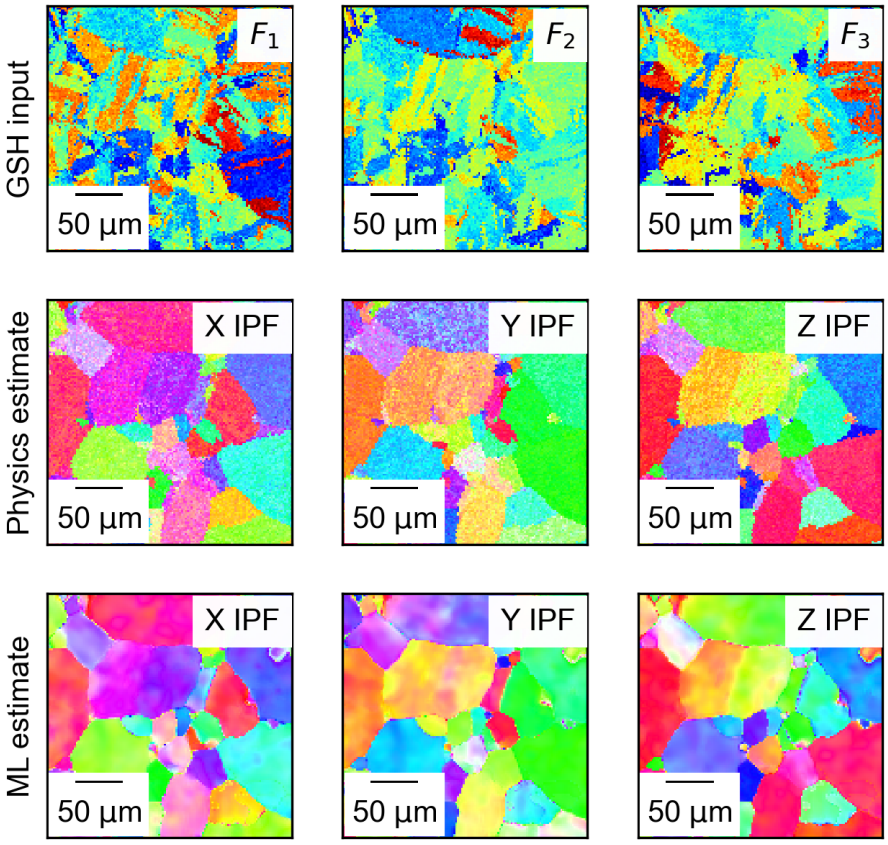

Figure 6: Validation data set example including several large scale grains.

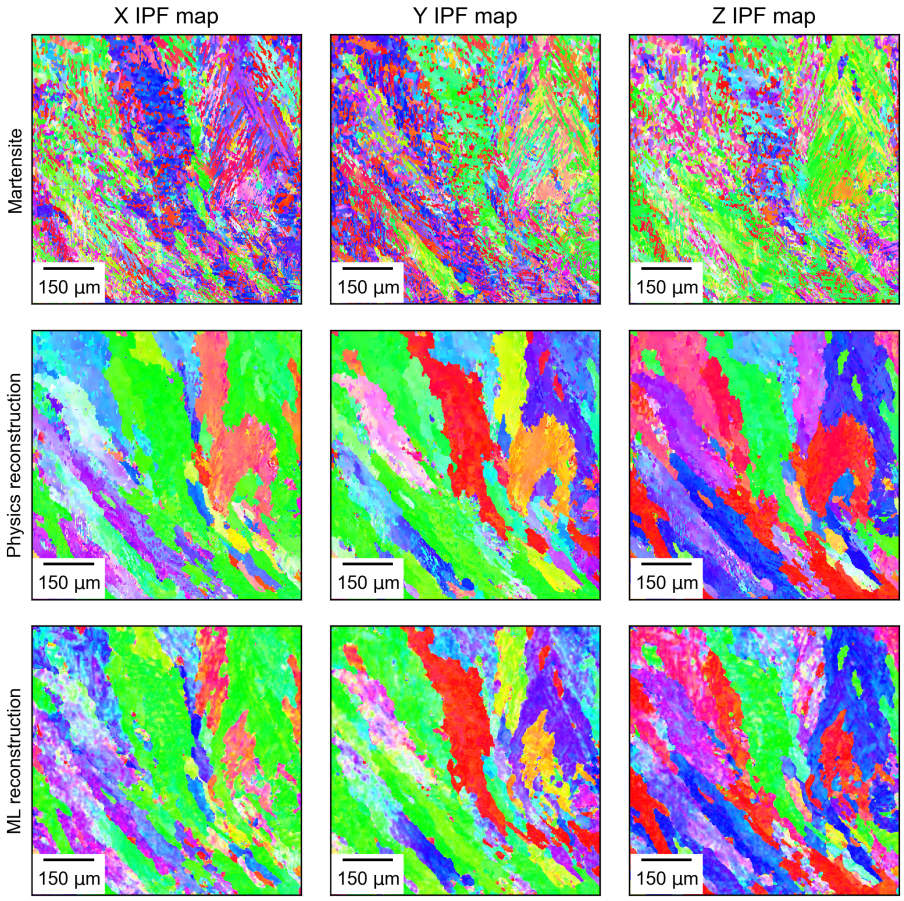

Figure 7: Test example on large area wire-arc AM 17-4PH material. The micrograph has a $1\,\mu m$ resolution.

the value of the central pixel. The model can "look" in the surrounding area and identify KS OR grain boundaries or boundaries far from being KS OR. It seems intuitive that when there are more features in the receptive field the model can more confidently infer the parent austenite grain orientation.

To demonstrate the importance of the receptive field now consider the higher magnification micrograph in Fig. 9. In each image a 128×128 pixel box is shown for reference. The original image in this case is 1536×1024 pixels with a $0.15\mu m$ pixel resolution. The micrograph only consists of fewer than 10 prior austenite grains. So in this case, there are very few grains in the receptive field of the model and the ML model exhibits poor predictive performance. As the resolution is decreased the model prediction becomes increasingly better. From this example it is clear that the limitation of the ML model is related to the perceptive field which is critical in capturing spatial-orientation patterns that drive the reconstruction. However, even in the highest resolution images small grains and small features, presumably those which fit inside the perceptive field, can still be predictive reasonably well. Even the large green grain is predicted reasonably well despite the magenta grain being poorly predicted. Visually it seems as though the green grain has many more lathe variants within it and so this potentially aids in inference. The magenta grain only consists of one martensitic variant. This suggests that the efficacy of inference is dependent on the degree of *microstructural information* present within the receptive field.

4. Discussion

In the prior section it was demonstrated that the established ML CV model is effective in generating reconstructed prior austenite orientation maps. When tested on unobserved 17-PH AM material with large morphologically anisotropic grains the model exhibited a remarkable ability to correctly infer the prior austenite structure at various pixel resolutions. However, it was empirically observed that for high magnification micrographs the model's performance greatly deteriorates. It is suspected that this is related to the receptive field of the model and the necessity for it to "see" sufficient contextual information for making accurate inferences.

Once again, in order to further analyze the performance of the model, we consider the full field prediction of the validation micrograph in Fig. 10. Two resolutions are shown: the native $0.5\mu m$ resolution and the $2\mu m$ resolution adopted for training. While the $0.5\mu m$ resolution estimate captures most of the grain structure and orientation it is heavily corrupted by spurious noise. The $2\mu m$ resolution micrograph is much more visually appealing with the exception of some internal grain misorientations. Again, it must be noted, however, that it seems that these misorientations are not random but rather mimic noise present in the physics reconstruction. So even these misorientations indicate that the ML CV model is identifying physical patterns which are indeed present in the physics based inferred micrograph. 128×128 windows are shown in all micrographs to highlight the size of training examples used for estimation of the model's hyperparameters. This is relevant because we hypothesize that the receptive field must be on the order of 128×128 pixels (or smaller) since this is all the model had available during training. It seems unlikely that, when considering a particular pixel, the model will be able to consider information

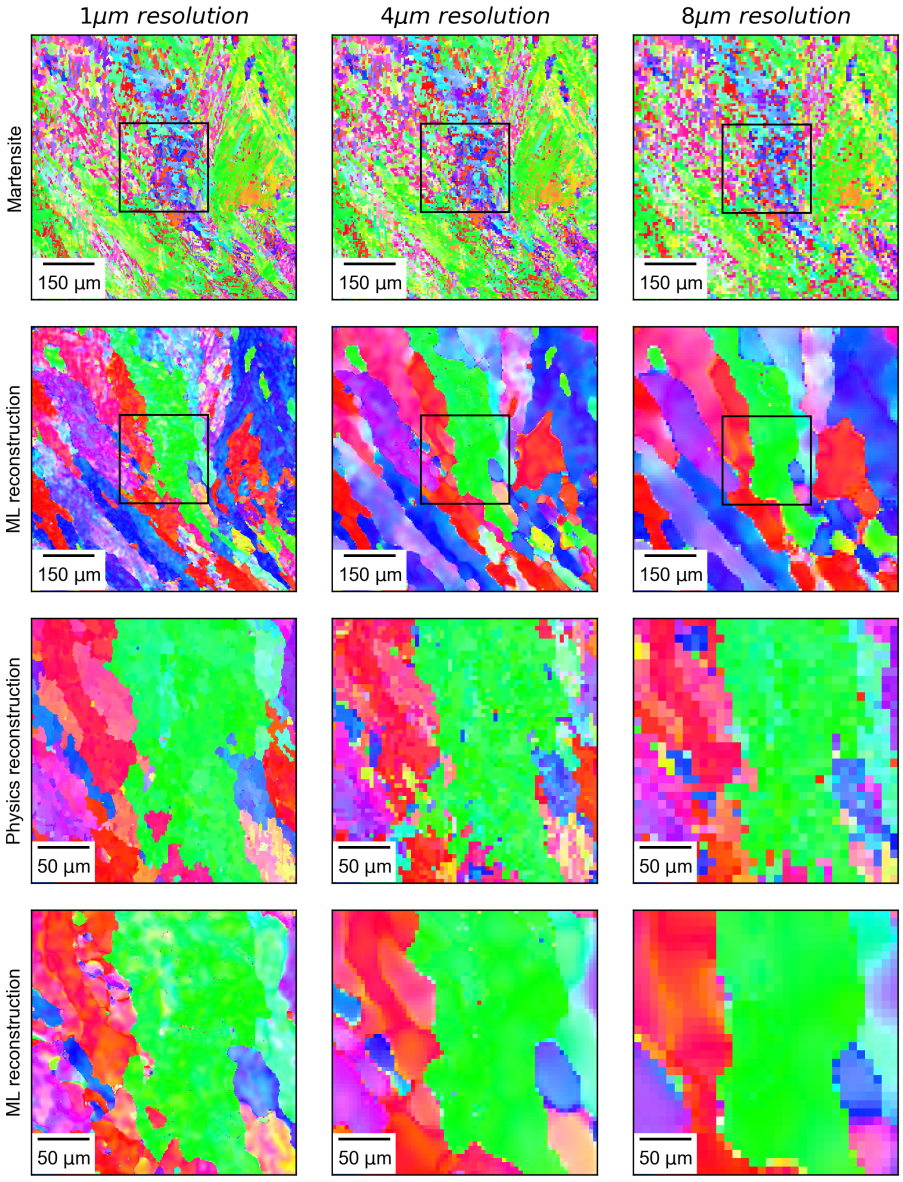

Figure 8: Micrographs demonstrating the effect of resolution and scale on large area wire-arc AM 17-4PH material. A selected area is shown to reveal smaller scale features.

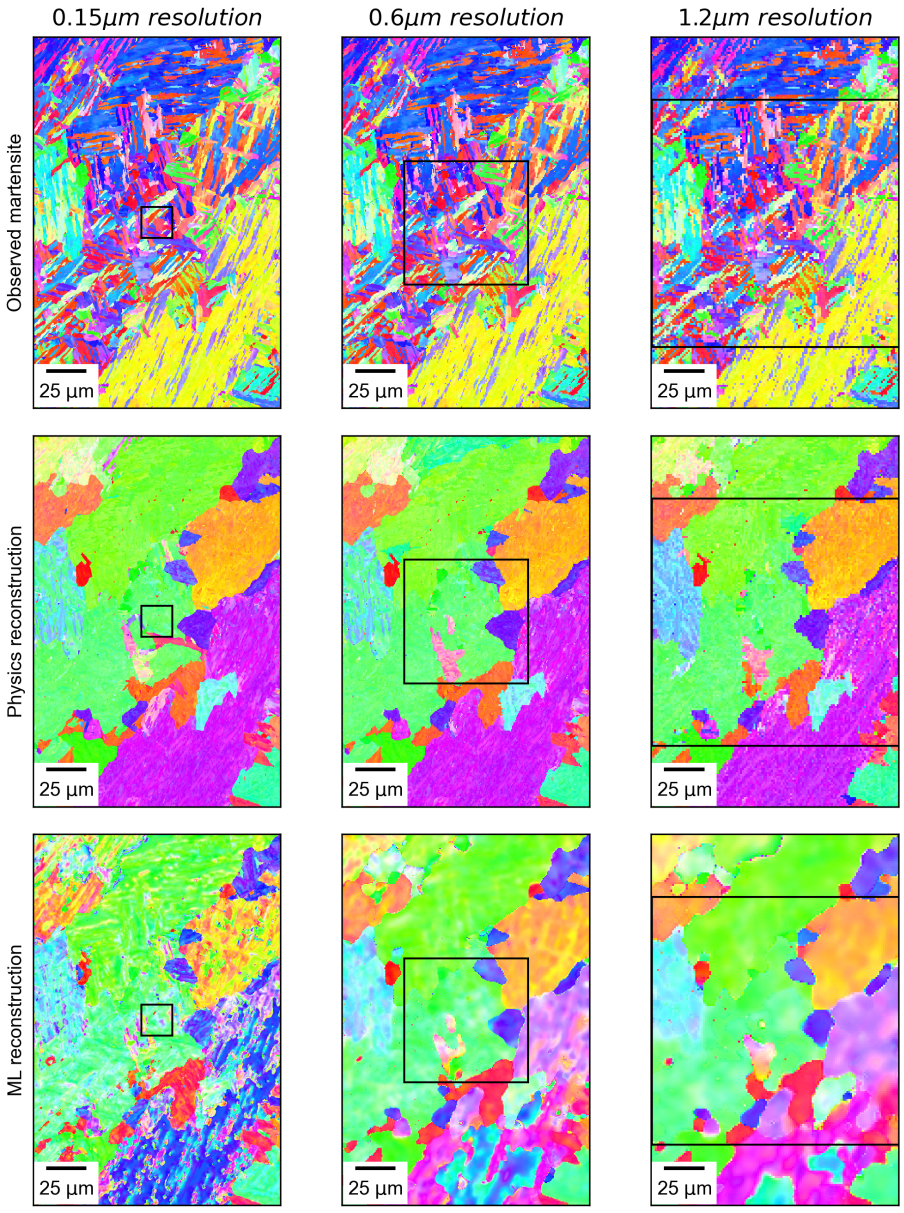

Figure 9: Micrographs demonstrating the effect of resolution and scale on small area wire-arc AM 17-4PH material.

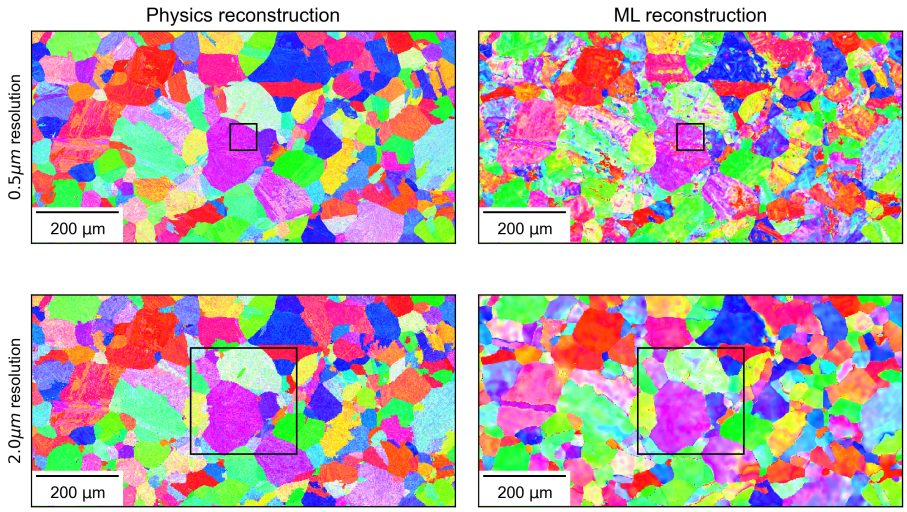

Figure 10: Difference in model predictions on the validation EBSD micrograph at resolutions $1\mu m$ and $2\mu m$. A 128×128 window, the size selected for training at $2\mu m$ resolution, is shown in each IPF map for perspective.

outside of this window size since such long range information was never present during training.

It is important to acknowledge that microstructural "features" are also necessary to consider. A pixel in the middle of a large grain will be more difficult to predict accurately if the grain is 500 pixels wide or 50 pixels wide. Hence, in Fig. 11 a more quantitative assessment of this concept is illustrated. The validation micrograph from Fig. 10 was manipulated to produce identical micrographs but at differt resolutions. We varied the resolution by fifteen factors yielding resolutions ranging from $0.25\mu m$ to $2\mu m$. Since the high resolution images grow large in pixel size not all the images could be processed fully and so we randomly sampled 128×128 patches 100 times at each resolution, predicted the prior austenite map using our ML model, and from that computed the GSH reconstruction error. The micrograph used for these operations contains 366 prior austenite grains and so given this, the known resolution of an image, and the use of a fixed 128×128 field of view, one can compute a summary metric which measures the influence of features present in the field of view against model error.

The results of this exercise agree with observations made previously in the manuscript; the model is effective in analyzing medium to low magnification micrographs but poor at high magnifications when there are few features available in the receptive field. This behavior was already observed before in Fig. 9 when the ML prediction was observed to improve at $0.6\mu m$ and $1.2\mu m$ resolution. The key consideration is the amount of microstructural feature information present within the receptive field of the model.

It may be possible to alleviate some of the model's deficiencies via adoption of alternative architectures or training strategies. There are a host of novel ML architectures that may be better suited for expanding the receptive field of

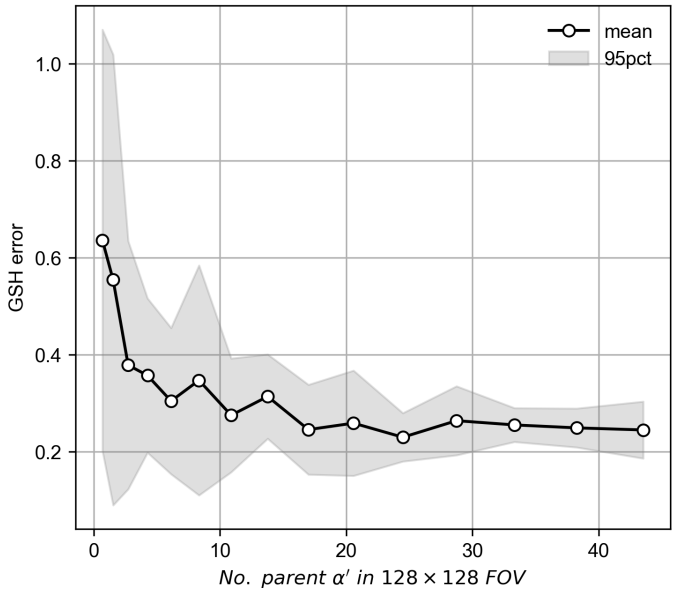

Figure 11: Mean error in the GSH representation prediction, $\|\boldsymbol{y}_{G,i} - \hat{\boldsymbol{y}}_{G,i}\|^2$, as a function of the number of parent α' grains in a 128×128 field of view (FOV). The gray region represents the 95% confidence interval computed from 100 random samples of the validation data.

the model to enable better generalization. Vision transformers are promising as they currently exhibiting great success in a number of vision related tasks [10]. Nonetheless, this work represents a first for successful application of ML CV models towards the analysis of experimental spatial orientation EBSD data. Furthermore, we demonstrate that we did not need a voluminous data set to effectively train the model; it was all done from only four micrographs. While the application of quantitative ML models directly on EBSD data has historically been made difficult due to issues associated with the orientation representation (Bunge-Euler angles) this complexity is precisely what enabled efficient training. The complexity of the data also makes it very dense and rich with information suitable for training complex models.

In order to develop a better understanding of the information flow through the model a few select feature maps corresponding to the top left corner of the validation micrograph are shown in Fig. 12. The top row corresponds to the input IPF map and then down sampled feature maps decreasing in resolution (left to right) through the U-net architecture. The bottom row corresponds to features in the up sampling portion of the model with resolution increasing (right to left) finally reaching the output IPF map. Interestingly, the lowest resolution map appears to have no discernible spatial structure. Across images and across filters, however, the mean value does change. This indicates that the deepest feature map simply captures some mean information. The first feature generated in down sampling almost always simply captures small length scale grain boundary features. It is likely that these maps are attempting to recognize "special" grain boundary relationships which may be related to near-KS OR features. The second down sampled map was empirically observed to capture both

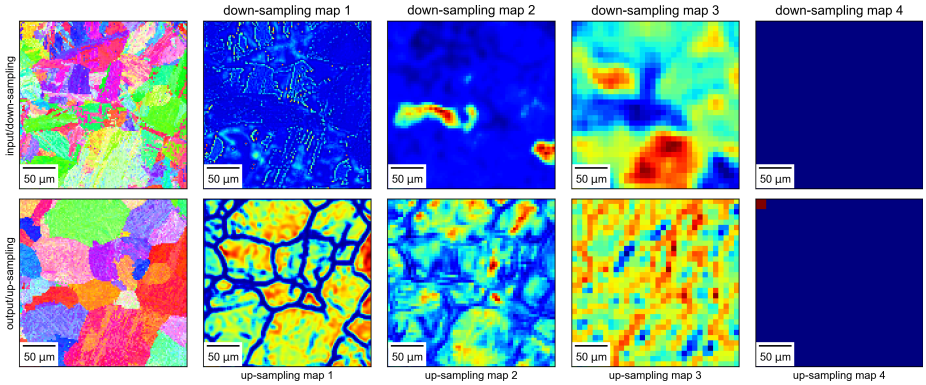

(a) Feature maps corresponding to filter 32.

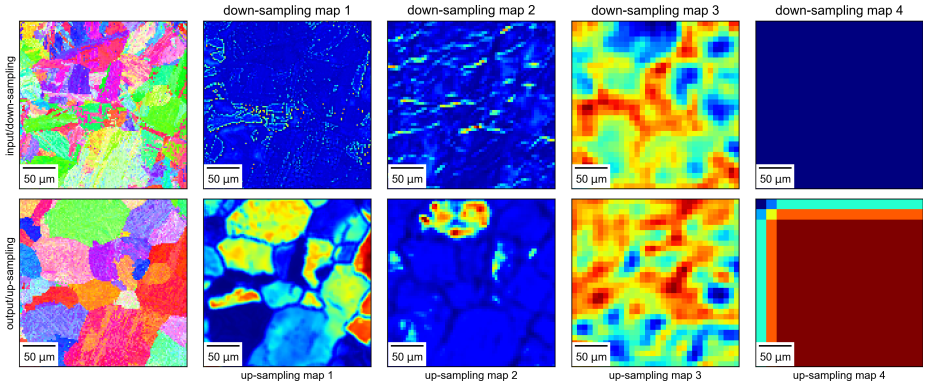

(b) Feature maps corresponding to filter 39

Figure 12: Feature maps produced during evaluation of the ML CV model.

boundary type information as well as grain features. The third down sampled maps are more difficult to interpret however they appear to capture long length scale features. The up sampling trends are once again similar with the exception that the up sampled map closest to the output is nearly entirely made up of grain scan features. Intuitively this agrees with the task that the model has been trained for; during down sampling select grain boundaries must be identified as well as long length scale features and during up sampling this information must be distilled into generating the parent austenite grain structure.

The direct value of this model is that it is incredibly fast. A visualization comparing the two methods, physics and ML models, is shown in Fig. 13. The physics based algorithmic approach utilized consistently requires significantly more time on the order of tens of minutes for inference. This is because the algorithms have to compute pixel-by-pixel misorientations, identify grain boundaries, identify martensitic grains, construct a graph connecting *all* martensite grains, etc.. Our ML model alleviates all of this by treating the problem much more locally and distilling all of these steps into a single computational pipeline. The result is that our ML model performs inference in less than a second even on the largest images considered ($768^2\, pixels$). Note, however, that these comparisons are somewhat unfair as the physics model is evaluated using CPU computations whereas the ML approaches takes advantage of the

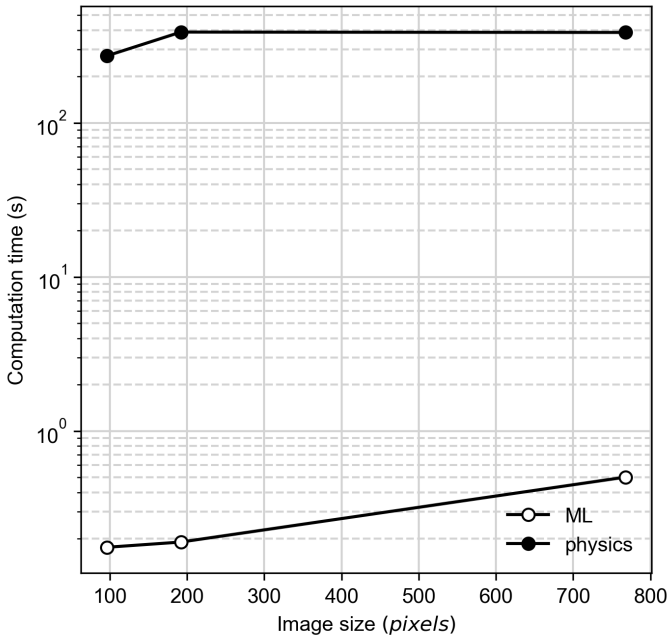

Figure 13: Computation time for physics and ML model.

computational efficiency of the GPU. Nonetheless, the speed of our ML CV model suggests that perhaps these reconstructions could be performed in real time. The computational efficiency is apparent and this aspect is attractive to microscopists and microscopy software developers who may see utility in being able to quickly preview the underlying prior austenite structure in-situ during imaging.

More generally, however, this work demonstrates that there is a viable framework for quantifying and analyzing EBSD micrographs using modern ML approaches. While we train this specific model to emulate an algorithmic physics-based model the framework can be generally applied towards other quantitative tasks. The value, demonstrated in the feature maps shown in Fig. 12, is that the GSH representation and CNN architecture are capable of encoding both local (grain boundary) and large length scale (shared γ parent grain) spatial-orientation features.

5. Summary

In this work we present a machine learning based computer vision model for reconstructing parent austenite grains from observed martensite EBSD micrographs. The model structure is based on a convolutional U-net architecture. The orientation data is represented using generalized spherical harmonics descriptors which alleviates issues associated with Bunge-Euler angles. Training of the model is performed using only four $\sim 1.0mm \times 0.5mm$ micrographs with a resolution of $2\mu m$ and this is achieved by utilizing a novel data augmentation strategy; randomization of the global reference coordinate system. Since the

global coordinate system is arbitrary this allows the model to "see" a much more diverse set of grain boundaries which facilitates in learning a more generalizable model. The model is shown to perform remarkably well when tested against martensitic micrographs obtained from a different alloy with completely different parent austenite grain structure. In addition, the evaluation of the model is orders of magnitude faster than algorithmic reconstruction approaches for large area micrographs. However, the model does have some limitations demonstrated by its poor performance when analyzing high resolution micrographs with few parent austenite grains. We suspect that this is related to the amount of microstructural information present in the receptive field of the model. This could be potentially alleviated by construction of alternative architectures.

6. Acknowledgements

Research was sponsored by the US Department of Energy, Office of Energy Efficiency and Renewable Energy (EERE), Advanced Manufacturing Office, the Office of Fossil Energy, Crosscutting Research Program, under contract DE-AC05-00OR22725 with UT-Battelle LLC and performed in partiality at the Oak Ridge National Laboratory's Manufacturing Demonstration Facility, an Office of Energy Efficiency and Renewable Energy user facility.

7. Competing Interests

The authors declare no competing interests.

8. Data availability

All data and models generated associated with the current study are available from the corresponding author request. The experimental data is publicly available at `https://petreldata.alcf.anl.gov/` [32].

9. References

References

[1] M. Abadi, P. Barham, J. Chen, Z. Chen, A. Davis, J. Dean, M. Devin, S. Ghemawat, G. Irving, M. Isard, et al. Tensorflow: A system for large-scale machine learning. In *12th {USENIX} symposium on operating systems design and implementation ({OSDI} 16)*, pages 265–283, 2016.

[2] M. Abbasi, T. W. Nelson, C. D. Sorensen, and L. Wei. An approach to prior austenite reconstruction. *Materials characterization*, 66:1–8, 2012.

[3] M. Abbasi, D.-I. Kim, T. W. Nelson, and M. Abbasi. Ebsd and reconstruction of pre-transformation microstructures, examples and complexities in steels. *Materials characterization*, 95:219–231, 2014.

[4] D. W. Abueidda, S. Koric, N. A. Sobh, and H. Sehitoglu. Deep learning for plasticity and thermo-viscoplasticity. *International Journal of Plasticity*, 136:102852, 2021.

[5] A. A. Antonysamy, J. Meyer, and P. Prangnell. Effect of build geometry on the β-grain structure and texture in additive manufacture of ti6al4v by selective electron beam melting. *Materials characterization*, 84:153–168, 2013.

[6] F. Bachmann, R. Hielscher, and H. Schaeben. Texture analysis with mtex–free and open source software toolbox. In *Solid State Phenomena*, volume 160, pages 63–68. Trans Tech Publ, 2010.

[7] S. Bi, J. Zhang, and G. Zhang. Scalable deep-learning-accelerated topology optimization for additively manufactured materials. *arXiv preprint arXiv:2011.14177*, 2020.

[8] H.-J. Bunge. *Texture analysis in materials science: mathematical methods*. Elsevier, 2013.

[9] C.-T. Chen and G. X. Gu. Generative deep neural networks for inverse materials design using backpropagation and active learning. *Advanced Science*, 7(5):1902607, 2020.

[10] A. Dosovitskiy, L. Beyer, A. Kolesnikov, D. Weissenborn, X. Zhai, T. Unterthiner, M. Dehghani, M. Minderer, G. Heigold, S. Gelly, et al. An image is worth 16x16 words: Transformers for image recognition at scale. *arXiv preprint arXiv:2010.11929*, 2020.

[11] P. Fernandez-Zelaia and S. N. Melkote. Process-structure-property modeling for severe plastic deformation processes using orientation imaging microscopy and data-driven techniques. *Integrating Materials and Manufacturing Innovation*, 8(1):17–36, 2019.

[12] A. L. Frankel, R. E. Jones, C. Alleman, and J. A. Templeton. Predicting the mechanical response of oligocrystals with deep learning. *Computational Materials Science*, 169:109099, 2019.

[13] S. Gupta, A. Banerjee, J. Sarkar, M. Kundu, S. K. Sinha, N. Bandyopadhyay, and S. Ganguly. Modelling the steel microstructure knowledge for in-silico recognition of phases using machine learning. *Materials Chemistry and Physics*, 252:123286, 2020.

[14] K. He, X. Zhang, S. Ren, and J. Sun. Deep residual learning for image recognition. In *Proceedings of the IEEE conference on computer vision and pattern recognition*, pages 770–778, 2016.

[15] D. Jha, S. Singh, R. Al-Bahrani, W.-k. Liao, A. Choudhary, M. De Graef, and A. Agrawal. Extracting grain orientations from ebsd patterns of polycrystalline materials using convolutional neural networks. *Microscopy and Microanalysis*, 24(5):497–502, 2018.

[16] K. Kaufmann, C. Zhu, A. S. Rosengarten, D. Maryanovsky, T. J. Harrington, E. Marin, and K. S. Vecchio. Crystal symmetry determination in electron diffraction using machine learning. *Science*, 367(6477):564–568, 2020.

[17] K. Kaufmann, H. Lane, X. Liu, and K. S. Vecchio. Efficient few-shot machine learning for classification of ebsd patterns. *Scientific reports*, 11 (1):1–12, 2021.

[18] D. P. Kingma and J. Ba. Adam: A method for stochastic optimization. *arXiv preprint arXiv:1412.6980*, 2014.

[19] A. Mangal and E. A. Holm. Applied machine learning to predict stress hotspots i: Face centered cubic materials. *International Journal of Plasticity*, 111:122–134, 2018.

[20] D. Montes de Oca Zapiain, A. Shanker, and S. Kalidindi. Convolutional neural networks for the localization of plastic velocity gradient tensor in polycrystalline microstructures. *Journal of Engineering Materials and Technology*, pages 1–41.

[21] M. Mozaffar, R. Bostanabad, W. Chen, K. Ehmann, J. Cao, and M. Bessa. Deep learning predicts path-dependent plasticity. *Proceedings of the National Academy of Sciences*, 116(52):26414–26420, 2019.

[22] T. Nyyssönen, P. Peura, and V.-T. Kuokkala. Crystallography, morphology, and martensite transformation of prior austenite in intercritically annealed high-aluminum steel. *Metallurgical and Materials Transactions A*, 49(12): 6426–6441, 2018.

[23] A. D. Orme, I. Chelladurai, T. M. Rampton, D. T. Fullwood, A. Khosravani, M. P. Miles, and R. K. Mishra. Insights into twinning in mg az31: a combined ebsd and machine learning study. *Computational Materials Science*, 124:353–363, 2016.

[24] N. H. Paulson, M. W. Priddy, D. L. McDowell, and S. R. Kalidindi. Reduced-order structure-property linkages for polycrystalline microstructures based on 2-point statistics. *Acta Materialia*, 129:428–438, 2017.

[25] N. H. Paulson, M. W. Priddy, D. L. McDowell, and S. R. Kalidindi. Data-driven reduced-order models for rank-ordering the high cycle fatigue performance of polycrystalline microstructures. *Materials & Design*, 154:170–183, 2018.

[26] O. Ronneberger, P. Fischer, and T. Brox. U-net: Convolutional networks for biomedical image segmentation. In *International Conference on Medical image computing and computer-assisted intervention*, pages 234–241. Springer, 2015.

[27] L. Scime and J. Beuth. Using machine learning to identify in-situ melt pool signatures indicative of flaw formation in a laser powder bed fusion additive manufacturing process. *Additive Manufacturing*, 25:151–165, 2019.

[28] L. Scime, D. Siddel, S. Baird, and V. Paquit. Layer-wise anomaly detection and classification for powder bed additive manufacturing processes: A machine-agnostic algorithm for real-time pixel-wise semantic segmentation. *Additive Manufacturing*, 36:101453, 2020.

[29] C. Shen, C. Wang, M. Huang, N. Xu, S. van der Zwaag, and W. Xu. A generic high-throughput microstructure classification and quantification method for regular sem images of complex steel microstructures combining ebsd labeling and deep learning. *Journal of Materials Science & Technology*, 2021.

[30] O. Sigmund and K. Maute. Topology optimization approaches. *Structural and Multidisciplinary Optimization*, 48(6):1031–1055, 2013.

[31] V. Sinha, M. Gonzales, and E. Payton. Datasets acquired with correlative microscopy method for delineation of prior austenite grain boundaries and characterization of prior austenite grain size in a low-alloy high-performance steel. *Data in brief*, 27:104471, 2019.

[32] V. Sinha, M. Gonzales, and E. Payton. Correlative microscopy data for quantification of prior austenite grain size in af9628 steel. `https://petreldata.alcf.anl.gov/mdf/detail/sinha_correlative_microscopy_steel_v1.1/`, 2019. [Online; accessed 13-April-2019].

[33] Y. Tan, B. Jin, A. Nettekoven, Y. Chen, Y. Yue, U. Topcu, and A. Sangiovanni-Vincentelli. An encoder-decoder based approach for anomaly detection with application in additive manufacturing. In *2019 18th IEEE International Conference On Machine Learning And Applications (ICMLA)*, pages 1008–1015. IEEE, 2019.

[34] J. Tiley, A. Shiveley, A. Pilchak, P. Shade, and M. Groeber. 3d reconstruction of prior β grains in friction stir–processed ti–6al–4v. *Journal of microscopy*, 255(2):71–77, 2014.

[35] K. Tsutsui, H. Terasaki, K. Uto, T. Maemura, S. Hiramatsu, K. Hayashi, K. Moriguchi, and S. Morito. A methodology of steel microstructure recognition using sem images by machine learning based on textural analysis. *Materials Today Communications*, 25:101514, 2020.

[36] P. Virtanen, R. Gommers, T. E. Oliphant, M. Haberland, T. Reddy, D. Cournapeau, E. Burovski, P. Peterson, W. Weckesser, J. Bright, et al. Scipy 1.0: fundamental algorithms for scientific computing in python. *Nature methods*, 17(3):261–272, 2020.

[37] Y. C. Yabansu, D. K. Patel, and S. R. Kalidindi. Calibrated localization relationships for elastic response of polycrystalline aggregates. *Acta Materialia*, 81:151–160, 2014.

[38] Z. Yang, Y. C. Yabansu, R. Al-Bahrani, W.-k. Liao, A. N. Choudhary, S. R. Kalidindi, and A. Agrawal. Deep learning approaches for mining structure-property linkages in high contrast composites from simulation datasets. *Computational Materials Science*, 151:278–287, 2018.

[39] Z. Yang, Y. C. Yabansu, D. Jha, W.-k. Liao, A. N. Choudhary, S. R. Kalidindi, and A. Agrawal. Establishing structure-property localization linkages for elastic deformation of three-dimensional high contrast composites using deep learning approaches. *Acta Materialia*, 166:335–345, 2019.

[40] Z. Yang, S. Papanikolaou, A. C. Reid, W.-k. Liao, A. N. Choudhary, C. Campbell, and A. Agrawal. Learning to predict crystal plasticity at the nanoscale: Deep residual networks and size effects in uniaxial compression discrete dislocation simulations. *Scientific reports*, 10(1):1–14, 2020.

[41] A. Zhang and D. Mohr. Using neural networks to represent von mises plasticity with isotropic hardening. *International Journal of Plasticity*, 132:102732, 2020.

[42] A. Ziabari, D. H. Ye, S. Srivastava, K. D. Sauer, J.-B. Thibault, and C. A. Bouman. 2.5 d deep learning for ct image reconstruction using a multi-gpu implementation. In *2018 52nd Asilomar Conference on Signals, Systems, and Computers*, pages 2044–2049. IEEE, 2018.

[43] A. Ziabari, M. Kirka, V. Paquit, P. Bingham, and S. Venkatakrishnan. X-ray ct reconstruction of additively manufactured parts using 2.5 d deep learning mbir. *Microscopy and Microanalysis*, 25(S2):376–377, 2019.

[44] A. Ziabari, S. Venkatakrishnan, M. Kirka, P. Brackman, R. Dehoff, P. Bingham, and V. Paquit. Beam hardening artifact reduction in x-ray ct reconstruction of 3d printed metal parts leveraging deep learning and cad models. In *ASME International Mechanical Engineering Congress and Exposition*, volume 84492, page V02BT02A043. American Society of Mechanical Engineers, 2020.